



LAWRENCE
LIVERMORE
NATIONAL
LABORATORY

First Principles-inspired Design Strategies for Graphene-based Supercapacitor Electrodes

B. C. Wood, T. Ogitsu, M. Otani, J. Biener

April 3, 2013

Journal of Physical Chemistry C

Disclaimer

This document was prepared as an account of work sponsored by an agency of the United States government. Neither the United States government nor Lawrence Livermore National Security, LLC, nor any of their employees makes any warranty, expressed or implied, or assumes any legal liability or responsibility for the accuracy, completeness, or usefulness of any information, apparatus, product, or process disclosed, or represents that its use would not infringe privately owned rights. Reference herein to any specific commercial product, process, or service by trade name, trademark, manufacturer, or otherwise does not necessarily constitute or imply its endorsement, recommendation, or favoring by the United States government or Lawrence Livermore National Security, LLC. The views and opinions of authors expressed herein do not necessarily state or reflect those of the United States government or Lawrence Livermore National Security, LLC, and shall not be used for advertising or product endorsement purposes.

First principles-inspired design strategies for graphene-based supercapacitor electrodes

Brandon C. Wood,^{1, a)} Tadashi Ogitsu,¹ Minoru Otani,² and Juergen Biener³

¹⁾*Quantum Simulations Group, Lawrence Livermore National Laboratory, Livermore, CA 94550*

²⁾*Nanosystem Research Institute, AIST, Tsukuba, Japan*

³⁾*Nanoscale Synthesis and Characterization Laboratory, Lawrence Livermore National Laboratory, Livermore, CA 94550*

Using density-functional theory calculations on a variety of model surfaces, we demonstrate that the low theoretical quantum capacitance of graphene-based electrodes can be significantly improved by altering local structural and morphological features. Common point defects, strain, and surface rippling are considered, as well as differences between locally single-layer and multilayer configurations. Local curvature-induced strain is particularly effective at improving quantum capacitance, as are Stone-Wales defects, and hydrogen adsorbed on dangling bonds. Single-layer graphene is found to exhibit poor screening behavior of the double-layer potential when compared with multilayer samples, suggesting higher area-specific capacitance can be obtained with samples a few layers thick. An approximation for the quantum capacitance based on a rigid shift of the density of states with applied bias proves reasonable for single-layer graphene, but breaks down for multilayer samples due to rehybridization of π^* states. Our results demonstrate the viability of local structural engineering as a tool to optimize graphene derivatives for use as supercapacitor electrodes.

I. INTRODUCTION

Supercapacitors have emerged as a highly promising device technology for temporary electrical storage, thanks to intrinsically high power densities that enable fast charging and discharging, as well as excellent cycling behavior. Ideal supercapacitor electrode materials should exhibit high electrical conductivity, high specific surface area and area-specific capacitance, as well as good mechanical strength, yet be chemically inert to ensure long device lifetime. For these reasons, sp^2 carbon materials have attracted a great deal of attention.¹⁻⁴ Nevertheless, limitations in the energy density of carbon-based supercapacitor electrodes remain a significant impediment.⁵

Besides development of advanced electrolytes, efforts towards increased capacitance have mostly been focused on optimizing the overall electrode morphology in order to increase the surface area and to take advantage of recently discovered pore size effects.^{2,6-8} The underlying notion is that energy storage nominally occurs in the electric double layer present at the electrode-electrolyte interface, and that the capacitance is therefore proportional to the active contact area. Furthermore, the capacitance of nanopores can depend strongly on the pore size; for example, it has been shown to increase threefold as the pores become smaller than the size of the solvated ion.⁷ However, it is important to emphasize that a strategy based exclusively on increased electrode-electrolyte contact area and pore morphology neglects the crucial role played by the electronic structure of the carbon electrode itself.

The importance of electronic structure in determining the area-specific capacitance of an electrode/electrolyte interface has been suggested in the past.^{9,10} It is also an accepted concept in the field of electrochemically gated graphene-based field-effect transistor devices.¹¹ However, in the field of electrochemical supercapacitors, the effect of quantum capacitance on device performance has attracted surprisingly little attention. This is despite its increasing relevance as high surface-area synthesis techniques improve and traditional morphological limitations are overcome.¹²⁻¹⁵ As an example, a recently synthesized graphene-derived electrode demonstrated an active, electrolyte-accessible surface area approximating that of a mass-equivalent graphene sheet, with both top and bottom electrode surfaces in contact with the electrolyte solution.^{5,16} Nevertheless, the area-specific capacitance was shown to decrease with increasing active surface area, in direct conflict with predictions based solely on electrode morphology.^{4,5} Based on these and similar results, it is clear that a new improvement strategy that directly accounts for the intrinsic electronic structure of the electrode is required.

This paper uses first-principles calculations on a variety of model systems in order to explore the nature and origin of intrinsic limitations in the capacitance of graphene-derived carbon electrodes, as well as to suggest strategies for improvement. We show that the capacitance limitation of graphitic carbon-based electrodes is indeed traceable to low electrode quantum capacitance as the limit of single-layer, graphene-like local morphology is approached, which directly illustrates the lack of available states for carriers to occupy upon charging. More significantly, we show that the limiting low density of states, and thus the capacitance, can be enhanced by tuning the *local* defect structure, morphology, and thickness of a carbon-based electrode. By investigating and evaluating each of these possibilities independently, we

^{a)}Electronic mail: brandonwood@llnl.gov

attempt to provide a theory-inspired road map that may be used to devise coherent design strategies for improving the capacitance in graphene-derived electrode materials.

II. COMPUTATIONAL METHODS

Density functional theory (DFT) calculations were performed within the plane-wave pseudopotential formalism, as implemented in the Quantum-ESPRESSO code.¹⁷ Ultrasoft pseudopotentials¹⁸ were employed with plane-wave and charge-density cutoffs of 30 and 300 Ry, respectively. The Perdew-Burke-Ernzerhof (PBE) exchange-correlation functional was used.¹⁹ For the point defects, $3\sqrt{3} \times 3\sqrt{3}$ hexagonal supercells (54 carbon atoms) were used, with the lattice parameter fixed to that calculated value for pristine graphene (2.46 Å). For the rippled surfaces, 4×4 hexagonal supercells (32 carbon atoms) were used. Rippling was induced by decreasing the in-plane lattice parameter perpendicular to the zigzag direction, convoluting the out-of-plane coordinates with a sinusoidal variation, and relaxing the resulting structure within the compressed unit cell. The folded geometry was produced in a similar manner, using an orthorhombic $2\sqrt{3} \times 9$ supercell (8 atoms across, 104 atoms total). The cell was compressed parallel to the zigzag direction and relaxed after convoluting with a sinusoidal variation. The degree of compression was chosen such that the spacing between the folds matched the experimental interlayer spacing in graphite. For all other surfaces, including in-plane strain and thickness calculations, the primitive cell was used. The interplanar spacing of the multilayer samples was fixed to the experimental value. Except where indicated, all ionic degrees of freedom were relaxed to determine equilibrium structures. Relaxations were performed using a 12×12 in-plane \mathbf{k} -point mesh for the primitive cell, which was increased to 96×96 for accurate determination of the density of states for the final configuration. For larger supercells, this same \mathbf{k} -point mesh density was retained. A gaussian electronic smearing of 0.007 Ry was applied to aid \mathbf{k} -point convergence. For calculations under a fixed bias potential, the effective screening medium (ESM) method²⁰ was employed.

III. RESULTS

A. Definition of capacitance

The total capacitance of an electrode-electrolyte interface can be modeled as an equivalent series circuit of component capacitance contributions from the solid electrode (C_s) and the liquid electrolyte (C_ℓ , itself consisting of Helmholtz and diffuse regions).^{9,21} This series representation is used routinely in fields such as graphene-based transistor devices;¹¹ here we also apply it to supercapac-

itors. Within this model, the contributions sum as

$$C_{\text{total}}^{-1} = C_s^{-1} + C_\ell^{-1}, \quad (1)$$

from which it is clear that the smaller of the two component terms will limit the overall device capacitance. Note that this construct assumes that C_s and C_ℓ can be treated independently, whereas in practice, they demonstrate a complex and ill-understood interdependency.²¹ Nevertheless, we adopt this model as a useful first-order approximation for the purpose of devising improved electrode optimization strategies.

For a perfect screening medium such as an ideal metal, the intrinsic electrode capacitance is effectively infinite and does not play a role in determining the device capacitance, and excess charge remains confined to the surface. However, in carbon materials, perfect screening is not attainable. In this case, the electrode capacitance C_s is represented by the quantum capacitance C_q , which can be evaluated directly from the electronic density of states (DOS) at a given voltage V :

$$C_q(V) = \frac{\partial Q}{\partial V} = e^2 \times \text{DOS}(-Ve). \quad (2)$$

The above definition assumes the voltage V is referenced to the zero-bias Fermi level.

However, for supercapacitor applications, the most important limiting quantity is usually the total energy storage capacity. This quantity is based not on the differential capacitance, but rather on its value integrated over a complete charge/discharge cycle, assuming equilibrium conditions (i.e., slow charge/discharge). The integrated quantum capacitance is therefore given as a function of charging voltage by:

$$C_q^{\text{int}}(V) = \frac{Q}{V} = \frac{1}{Ve} \int_0^V C_q(V') dV'. \quad (3)$$

Because we are concerned primarily with providing guidelines for enhancing the energy density of graphene-based supercapacitors, we focus on the integrated capacitance in this paper.

Nevertheless, the differential and integrated capacitances are often mistakenly used interchangeably.^{22–24} This is in part because the two quantities are degenerate for ideal metallic electrode behavior. However, if the electrode behaves non-ideally, as is the case for graphene-based materials, it is important to distinguish between them when comparing theoretical predictions with experimental measurements. For instance, cyclic voltammetry and galvanostatic measurements can be used to derive the integrated or differential capacitance, whereas impedance spectroscopy is used to assess the differential capacitance.²³ Similarly, continuum capacitance models are generally based on integrated capacitance, yet first-principles calculations often report differential capacitance only.

In principle, the shape of the density of states in Eq. 2 depends implicitly on the charge, and by extension, the

voltage. However, for small bias, it is assumed that this dependence is minor, and that slow charging or discharging simply changes the Fermi occupation of an otherwise fixed density of states. We refer to this as the “fixed-band approximation,” within which all calculations presented here are performed unless otherwise indicated. It turns out that the validity of this approximation is limited to single-layer samples, as discussed below.

B. Pristine graphene

The area-specific and gravimetric quantum capacitance of pristine graphene for a ± 1.5 V range is shown in Fig. 1. The calculation is carried out within the fixed-band approximation, and shows both the integrated (Eq. 3) and differential (Eq. 2) capacitances. The difference between the two capacitances for graphene is clearly manifested: the near-linear dispersion of the DOS around the Fermi level translates to an integrated capacitance that is smaller than the differential value by about a factor of two. Note that energies below the Fermi level correspond to positive bias (electron depletion), whereas energies above the Fermi level correspond to negative bias (electron accumulation).

Looking at the integrated capacitance, the results clearly demonstrate that for much of the ± 1.5 V range, the area-specific C_s is smaller than typical values of C_ℓ (Fig. 1 shows one example, for $C_\ell = 20 \mu\text{F}/\text{cm}^2$). This means that the total capacitance is indeed limited by the dearth of available states for electrons and holes near the Dirac point, as has been suggested.^{5,9,10,25} To further illustrate this point, we computed the capacitance of a fictitious graphene-equivalent electrode that has a constant DOS instead of the known linear dispersion. The constant DOS resembles an ideal 2-D free electron system in which the charge remains confined to the surface. A graphene unit cell was assumed, with the DOS from the minimum valence level to the Fermi level replaced by its average value over that range. In this case, Fig. 1 shows that the integrated and differential capacitances have an identical value that is significantly greater than the typical C_ℓ , such that the latter becomes limiting.

Note that the value of C_q^{int} in Fig. 1 at 0 V is nonzero. The reason for this is twofold. First, electronic smearing is employed to limit the size of the \mathbf{k} -point mesh. This imposes an effective temperature on the electrons (1100 K) and removes the ideal behavior at the Dirac point. (We note that experimental measurements should exhibit a similar but lesser effect if performed at room temperature.) Second, there are intrinsic numerical inaccuracies associated with dividing two near-zero quantities in Eq. 3, making reliable calculation near 0 V difficult for samples with low densities of states at the Fermi level.

The capacitance in Fig. 1 is generally higher at negative bias (i.e., testing unoccupied states above the Fermi level) than at equivalent positive bias, in agreement with experiments.²⁶ The difference is relatively minor for small

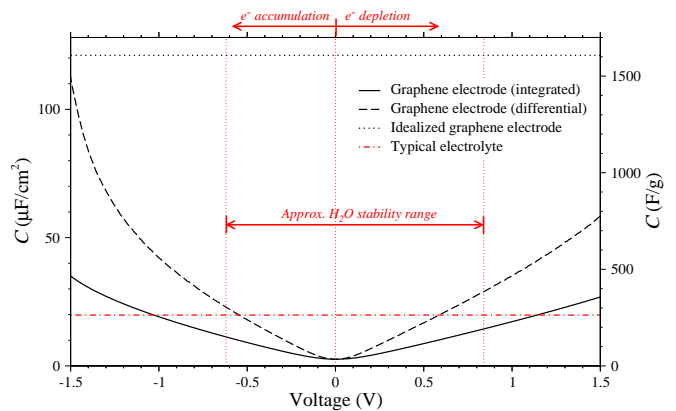


FIG. 1: Comparison of theoretical integrated (solid black line) and differential (dashed black line) quantum capacitance for pristine graphene, calculated within the fixed-band approximation. The dotted black line shows the result for a fictitious idealized graphene in which the electronic DOS is replaced with a constant value for all energies above the minimum occupied valence level. Here, the constant DOS value represents the average graphene DOS over all energies from the minimum occupied valence level to the zero-bias Fermi level. For the fictitious system, the integrated and differential capacitances are degenerate. A typical area-specific double-layer capacitance of $C_\ell = 20 \mu\text{F}/\text{cm}^2$ is shown for reference (dash-dotted red line).

voltages, but becomes quite large beyond ± 0.6 V, due to the breakdown in the linear dispersion at negative bias. In the region where the dispersion remains approximately linear (say, from -0.5 V to 0.5 V), we can fit the differential quantum capacitance data to the analytical expression for the linear-dispersion quantum capacitance. This allows us to extract the equivalent Fermi velocity v_F . In the limit of zero temperature, the quantum capacitance expression for a linear dispersion DOS becomes²⁷

$$C_q(V) \approx \left| \frac{2e^3 V}{\pi \hbar^2 v_F^2} \right|. \quad (4)$$

Using Eq. 4 and performing a linear regression of the differential capacitance data in Fig. 1, we obtain a Fermi velocity of 8.2×10^5 m/s. Although in good agreement with other generalized gradient-based DFT methods,²⁸ this value is 18–29% smaller than values reported in the literature.^{26,29–34} There are a few potential reasons for the experiment-theory discrepancy. First, PBE could be underestimating the Fermi velocity due to improper description of nonlocal exchange, as has been suggested previously.^{28,35} Second, the fixed-band approximation used in our study does not account for the presence of the electrolyte and the interfacial electric field, and may therefore be overestimating the capacitance. Third, intrinsic defects are introducing additional carriers in the region near the Fermi level in the experiments, which has the effect of increasing the observed Fermi velocity in that

region. Further study is required to determine which combination of these forms the dominant contributor.

C. Thickness dependence and screening behavior

The experimentally observed decrease in area-specific capacitance near the single-layer limit⁵ suggests that excess charge induced on a graphene substrate may not be effectively screened within the electrode. This relates to the low concentration of surface states for pristine single-layer graphene, as shown in Fig. 1. In this event, there may be a benefit to using multilayer graphene structural units to realize higher area-specific quantum capacitance, as the additional layers can contribute to the image charge. Additional layers could be especially valuable when both faces of the electrode are simultaneously exposed to the electrolyte, as in most electrode designs.

Although it is possible to perform a straightforward fixed-band quantum capacitance calculation for multilayer graphene, this would not directly (or indirectly) account for the presence of the electrolyte-induced electric double layer (EDL). The EDL induces a field at the interface that decays into the electrode. In multilayer electrodes, the outer layers see a different potential from the inner layers, with the degree of the difference determined by the screening properties of the electrode. It is therefore useful to gain a measure of the extent of the screening length. From this, we can derive the minimum thickness for near-complete screening of an interfacial double layer, and consequently of maximal area-specific capacitance.

We evaluate the electrode screening properties as a function of layer thickness using the Effective Screening Medium (ESM) method.²⁰ The ESM method modifies the Hartree potential via a Green's function formalism to simulate insertion of the electrode slab between two virtual media with specified dielectric constants. We polarize the slab by applying a fixed electric field of 0.4 V/\AA between the two virtual infinite-dielectric perfect metals. This is comparable to the interfacial field strength generated by the EDL. The decay of the polarization response into the interior of the multilayer electrode slab is then used to obtain a measure of the Debye-Hückel screening length.

Figure 2 shows the response of the charge density to the application of the electric polarization field as a function of slab thickness. We use ABA stacking for all samples. It is immediately obvious that for thinner slabs, the polarization response does not fully decay within the electrode. This is a manifestation of the low density of surface states, which forces displaced charge to the inner electrode layers. Beginning with the six-layer slab, screening behavior improves significantly. For the thicker slabs, the decay of the polarization response can be fit to an exponential curve. For a field strength of 0.4 V/\AA , the $1/e$ screening length is found to be 2.2 \AA . To obtain a 95% screening of the polarization response therefore requires 6.6 \AA of material, which corresponds to about two addi-

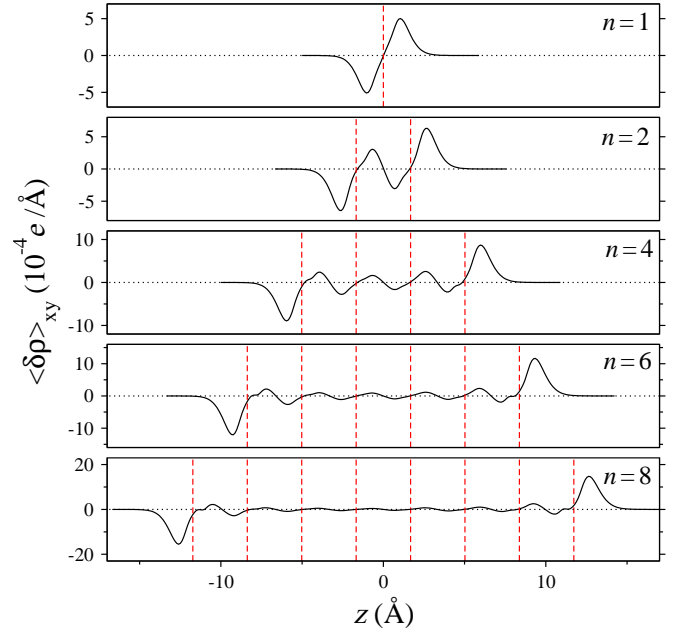


FIG. 2: Charge density accumulation or depletion upon application of an electric field (0.4 V/\AA) perpendicular to n stacked graphene layers, shown as a function of slab thickness. Results for $n=1, 2, 4, 6$, and 8 are shown.

In each case, the density is averaged parallel to the graphene basal plane. The red dashed lines indicate the positions of the graphene layers.

tional layers beyond the surface. This should be doubled for supercapacitor operation in which the both surfaces are assumed to be in contact with the electrolyte, meaning graphitic electrodes should be at least five or six layers thick in order to generate the highest area-specific capacitance. However, for actual device engineering, this must be mediated by considerations of gravimetric and volumetric capacity, which will decrease with thicker samples.

The fact that successive layers in multilayer graphene experience a different potential under actual operation due to the presence of the electrolyte, as we have supposed, is borne out clearly in the ESM calculations of Fig. 2. This same approach allows us to evaluate the validity of the fixed-band approximation for calculating the quantum capacitance of multilayer slabs. In doing so, we find that the fixed-band approximation fails even for bilayer slabs, and more spectacularly for thicker slabs. This can be seen in Fig. 3, which plots the band structure of n -layer graphene for $n=1, 2$, and 8 before and after application of the electric polarization field. In order to permit direct comparison, we have aligned the zero of energy to the Fermi level in the absence of the electric field. For single-layer graphene, the band structure does not change upon application of the polarizing field, suggesting the fixed-band approximation holds well within the voltage range of interest. However, for bilayer and 8-layer graphene, the presence of the field breaks the symmetry and induces level splitting in the states nearest

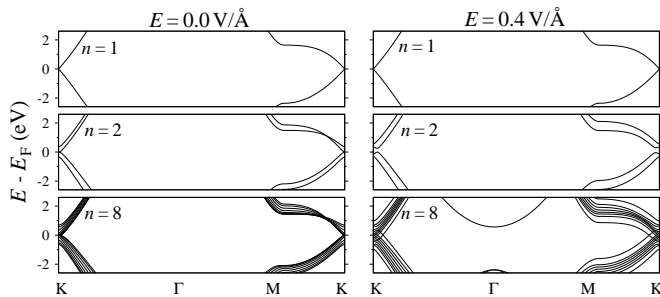


FIG. 3: Electronic band structure of n stacked graphene layers before (left panels) and after (right panels) application of an electric field (0.4 V/\AA). Results for $n=1, 2$, and 8 in the range $\pm 2.5 \text{ V}$ are shown. The zero of energy is aligned to the Fermi level in the absence of the electric field.

the Fermi level. For bilayer graphene, this opens a gap near the K point, as reported previously.^{36–38} For 8-layer graphene, the field-induced level splitting instead creates a near-continuum of bands. Interestingly, for the thicker slab, there is also a contribution to the density of states from the π^* states, which are driven lower in energy by the field until they mix with the states nearer the Fermi level. Although this shift of the π^* states is also seen for the thinner samples, its magnitude depends on the thickness (it is barely visible beyond $E - E_F = 2.0 \text{ eV}$ for the bilayer). It is worth noting that there is a corresponding shift of the π states upward towards the Fermi level; however, the degree of the shift is much smaller, and does not appear within the $\pm 2 \text{ V}$ window even for the 8-layer slab. A similar asymmetric π - π^* field response has been reported in recent experiments on bilayer graphene.^{37,38}

We emphasize that the rehybridization of states near the Fermi level for thicker slabs in Fig. 3 would not be captured in the fixed-band approximation, nor would the observed level splitting at the K point for multilayer slabs. Moreover, the response is asymmetric, with the π^* states apparently much more sensitive to an applied field than the π states. As such, detailed studies of the quantum capacitance of multilayer slabs should be done using more direct methods rather than relying on the fixed-band approximation. We are currently investigating this in detail. On the other hand, single-layer graphene can be adequately described within the fixed-band approximation for the voltage range of interest, at least for field strengths on the order of 0.4 eV/\AA . Naturally, the magnitudes of the level shifts in Fig. 3, as well as the observed screening length, should depend on the field strength. The dependence is likely quasi-linear, matching the behavior reported for screening radius in the basal plane.³⁹ In this regard, the fixed-band approximation could fail even for single-layer graphene at large field strengths. However, for most realistically achievable field strengths, this is unlikely to be the case. As such, we continue to rely on the fixed-band approximation for the structures in the remainder of this paper, all of which are derived

from single-layer geometries.

D. Point defects

Several experimental measurements of the capacitance of single-layer graphene have exhibited significant deviations from the zero-temperature ideal limit, and from the pristine graphene behavior shown in Fig. 1.^{26,29,30,40,41} Common features include a significantly enhanced, nonzero density of states at the Fermi level, and enhanced capacitance at potentials close to zero bias that is largely flat across a range of tens or hundreds of meV. This leads to better-than-predicted capacitive behavior in this region, which authors have generally attributed to additional states due to defects or local electronic density oscillations. In other words, the electronic signature of graphene implies that it is unlikely to retain a zero-temperature, defect-free structure under actual testing conditions. It is reasonable to assume that this effect will be amplified in intrinsically defect-rich systems, such as polymer-derived, three-dimensional graphene structures.¹⁶ Selective and deliberate inclusion of certain defects through controlled synthesis may therefore be used as a tool to enhance the quantum capacitance. Accordingly, we devote the following sections to a detailed analysis of the effects of local modifications to graphene-based materials.

We begin with a discussion of graphene point defects. A variety of native point defects have been recorded in graphene samples, including the Stone-Wales defect (55–77), various divacancy structures (e.g., 5–8–5 and 555–777), and monovacancies (5–9).^{36,42} Models of graphene in the presence of these defects are depicted in Fig. 4. Each was tested for its effect on the quantum capacitance of a graphene electrode within the fixed-band approximation. In the case of the monovacancy, a Jahn-Teller distortion creates a five-membered ring via an elongated bond between two of the carbons nearest the vacancy. This leaves the third carbon with an exposed dangling bond that is similar to a zigzag edge, which we also tried passivating with hydrogen or oxygen. Of the tested defects, only the unpassivated monovacancy possesses a nonzero magnetic moment, although this is removed upon addition of hydrogen or oxygen.

The calculated quantum capacitance upon selective introduction of each of the point defects in a 54-atom supercell is shown in Fig. 5. It is immediately evident that the addition of defects can increase the capacitance profile considerably. The degree to which this is the case depends both on the defect species and on the applied potential; however, in almost all instances, the effect is to increase C_q^{int} with respect to the graphene baseline. Particularly large contributions near the Fermi level are observed for the 555–777 divacancy and for the 5–9 monovacancy in the presence of a hydrogen. The capacitance profile of these two look very similar across the voltage range in the Figure, with additional increases in C_q^{int} ex-

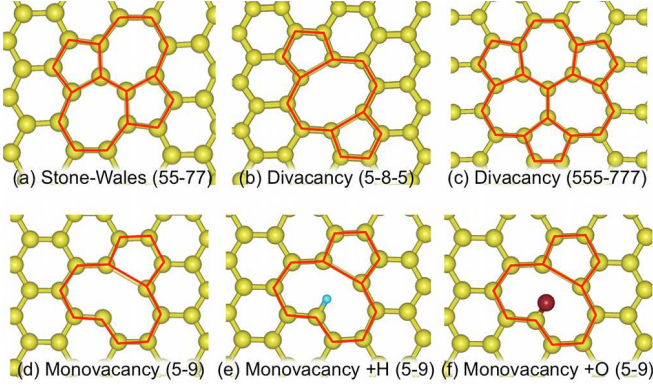


FIG. 4: Types of native graphene point defects considered in the present study.

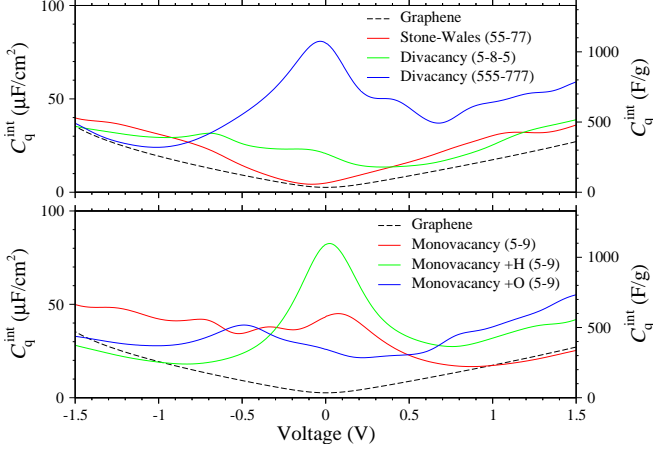


FIG. 5: Theoretical integrated quantum capacitance C_q^{int} of graphene upon addition of the point defects in Fig. 4. A fixed defect concentration of one defect per 54 carbon atoms ($7 \times 10^{13} \text{ cm}^{-2}$) was used.

pected at positive potentials.

The unpassivated monovacancy enhances C_q^{int} under negative bias, but has little effect at positive voltages beyond +0.5 V. Interestingly, this picture is reversed when the dangling bond is passivated either by hydrogen or oxygen, with enhancements instead appearing at positive voltages and tapering off at negative bias. The especially large contribution near the Fermi level from the hydrogen-passivated monovacancy resembles similar calculations of hydrogen adsorption on pristine graphene,⁴³ and suggests that hydrogen chemisorption could contribute significantly to quantum capacitance in graphene derivatives with high concentrations of exposed edges or pores. Indeed, local chemical modification could represent a valuable engineering strategy; we are currently pursuing this research direction. Note that the 55–77 Stone-Wales defect is the only point defect we tested that did not appreciably change the density of states at the Fermi level. Nevertheless, it does increase the observed C_q^{int} at nonzero bias in both positive and negative direc-

TABLE I: Defect formation energies ΔE_f for the point defects in Fig. 4, calculated within a 54-atom supercell with respect to pristine graphene. For the hydrogen/oxygen-passivated monovacancy, gas-phase molecular H_2/O_2 was used as a reference.

Defect	ΔE_f (eV)
Stone-Wales (55–77)	5.3
Divacancy (777–555)	7.2
Divacancy (5–8–5)	8.1
Monovacancy (5–9)	7.7
Monovacancy +H (5–9)	5.8
Monovacancy +O (5–9)	4.7

tions. This agrees with previous DOS calculations.^{43–45}

The models in Fig. 4 correspond to extremely high defect densities (one per 54 carbon atoms), making the enhancements with respect to pristine graphene appear especially large. These should be scaled to match observed concentrations. We show the calculated formation energies (based on the 54-atom supercell) for each of the point defects in Table I. The formation energies are calculated according to

$$\Delta E_f = E(\text{defect}) - \frac{m}{54} E(\text{graphene}) - \left\{ \frac{1}{2} E(\text{H}_2/\text{O}_2) \right\}, \quad (5)$$

where m represents the number of carbon atoms in the defective supercell. The last term applies only in the case of the hydrogen- and oxygen-adsorbed monovacancies, for which the energy of the reference H_2/O_2 gas must also be subtracted. Note that this definition in Equation 5 assumes a neutral electrode, in which the defect complexes are uncharged; allowing for charged defects will slightly shift some of the values in Table I.⁴⁵ The defect formation energies are sufficiently large that one should not expect significant enhancements in the C_q^{int} of pristine graphene from point defects at room temperature. However, for highly disordered graphene derivatives, this picture is likely to change, and the values in Table I become useful for gauging the relative contributions of the curves in Fig. 5. Because selective introduction of certain native point defects over others may be difficult, the results in this section are probably best examined collectively. Still, it is clear that the presence of defects generally increases the capacitance of graphene-based electrodes.

E. Local strain and curvature

Since the physical morphology of the electrode surface represents an additional possible variable in the processing of nanoporous carbon substrates, we also ran a series of simulations investigating the capacitance of curved and strained graphene surfaces.³⁶ The effects of in-plane

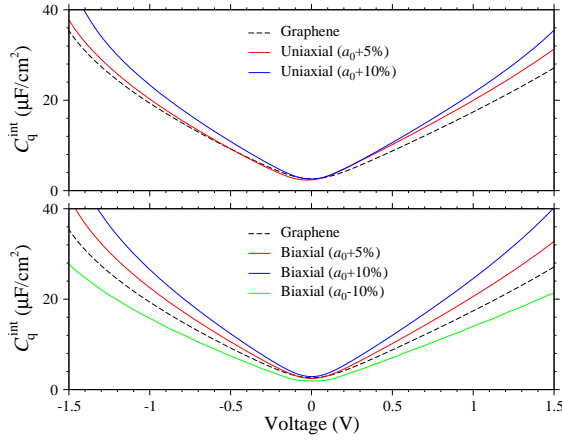


FIG. 6: Theoretical area-specific integrated quantum capacitance C_q^{int} of graphene upon application of in-plane uniaxial strain (top panel) and biaxial strain (bottom panel). For the uniaxial case, the strain was applied parallel to the zigzag direction. Results are shown for 5% and 10% linear expansion of the in-plane lattice parameter (5% and 10% areal increase for uniaxial strain; 10% and 21% areal increase for biaxial strain). For the biaxial case, results are also shown for an in-plane 10% linear compression in the lattice parameter (19% areal decrease).

strain were tested, as well as surface buckling under compression.

The changes in fixed-band capacitance upon application of high uniaxial strain applied parallel to the zigzag direction, and upon application of biaxial strain applied uniformly along both planar directions, are shown in Fig. 6. Linear expansions of the equilibrium in-plane lattice parameter by 5% and 10% were examined (for biaxial strain, these were applied equivalently in both in-plane directions). We also tested the case of biaxial compression based on a 5% linear contraction in the lattice parameter, under the constraint of no out-of-plane atomic rearrangement. We recognize that the magnitude of our applied strains are high, but they are illustrative for modeling purposes. In addition, the surface variations in nanoporous carbon, and the nonequilibrium process by which they are produced, are likely to generate local regions with higher-than-normal strain energy.

The results in Fig. 6 show a general trend of increased area-specific C_q^{int} with in-plane tensile strain. This is true even after accounting for the correspondingly enhanced surface area (the gravimetric C_q^{int} would show an even more dramatic effect). For the range of ± 1.5 V, the changes scale with voltage and with the level of applied strain. This agrees with previous calculations of reduced Fermi velocity in strained graphene.⁴⁶ The increase in C_q^{int} for biaxial expansion of the lattice parameter by 5% are approximately equal to the 10% uniaxial expansion case. Since these translate to essentially equivalent surface areas, this suggests that the directionality of the

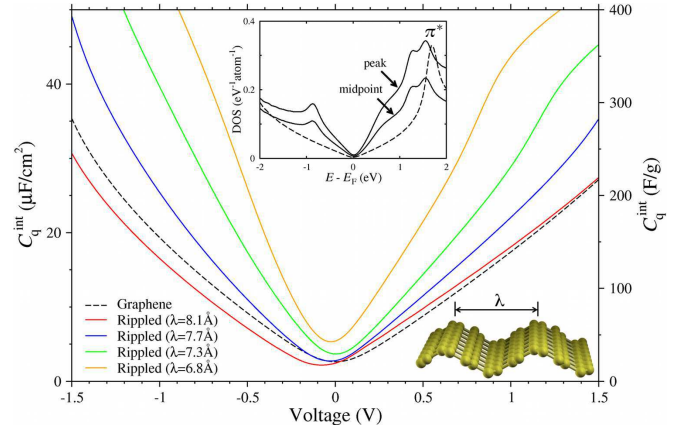


FIG. 7: Theoretical area-specific integrated quantum capacitance C_q^{int} of graphene upon surface rippling under compression. Results are shown for ripples of four different characteristic wavelengths ($\lambda = 6.8 \text{ \AA}$, 7.3 \AA , 7.7 \AA , and 8.1 \AA). The inset shows the density of states of rippled graphene ($\lambda = 6.8 \text{ \AA}$), projected onto a carbon atom at the peak of the ripple (point of highest curvature) and onto a carbon atom at the flattest midpoint between two successive peaks. In both the inset and the main figure, the dashed line indicates the result for pristine graphene.

applied strain is less important than the magnitude of the areal increase.

According to Fig. 6, in-plane compressive strain tends to dampen C_q^{int} with respect to pristine graphene. However, under compression, a graphene surface is known to corrugate in order to dissipate strain energy.⁴⁷ To simulate such corrugation, we compressed the cell along the zigzag direction and allowed for sinusoidal variation of the out-of-plane coordinates. Four different values of in-plane compression were explored (5%, 10%, 15%, and 20% linear compression), corresponding to different characteristic wavelengths λ of the sinusoidal surface ripples: $\lambda = 8.1 \text{ \AA}$, 7.7 \AA , 7.3 \AA , and 6.8 \AA . The resulting changes in C_q^{int} are shown in Fig. 7. The calculations demonstrate that a very large enhancement of the quantum capacitance can be realized upon rippling, and that this enhancement scales with curvature (inversely with wavelength). Note that the contribution to the capacitance is opposite in sign from what we saw for in-plane compression. Because surface buckling is a lower-energy transformation than in-plane compression, and because tension also enhances capacitance, strain of either sign is likely to be linked to increased quantum capacitance. Accordingly, electrodes should be engineered to maximize local variations in morphology in order to increase local strain magnitudes; planar geometries are inefficient by comparison.

Since even pristine graphene is known to exhibit corrugation by room-temperature activation of low-frequency modes,³⁶ it is reasonable to assume some degree of capac-

itive enhancement of the type seen in Fig. 7 should be present natively. As such, one should expect somewhat more aggressive scaling of C_q^{int} with voltage magnitude than is predicted for ideal graphene.

There are some characteristic features to note in the ripple-induced changes in fixed-band capacitance depicted in Fig. 7. A shoulder appears in the capacitance at positive bias, the location of which shifts towards smaller voltages with larger curvature (shorter wavelength). The location is at +2.0 V, +1.6 V, +1.2 V, and +0.9 V for $\lambda = 8.1 \text{ \AA}$, 7.7 \AA , 7.3 \AA , and 6.8 \AA , respectively. A soft shoulder can also be seen at negative bias for the highly corrugated samples, appearing around -0.5 V to -0.8 V for the highest corrugation ($\lambda = 6.8 \text{ \AA}$). In real nanoporous carbon samples, the features in Fig. 7 would be averaged over multiple curvatures, and would most likely manifest as a change in the slope of the capacitance.

These features can be seen more clearly in the inset of Fig. 7, which shows the density of states for one of the samples ($\lambda = 6.8 \text{ \AA}$), projected onto carbon atoms at the ripple peak, where the curvature is maximized, and at the flattest region, where the curvature is minimized. The feature at positive bias (below the Fermi level) appears as a peak at $E - E_F = -0.9 \text{ eV}$. At negative bias (above the Fermi level), there is a shoulder at $E - E_F = 0.6\text{--}0.9 \text{ eV}$, and the π^* peak ($E - E_F = 1.8 \text{ eV}$ for pristine graphene) shifts towards the Fermi level and splits into two peaks at $E - E_F = 1.2 \text{ eV}$ and 1.6 eV . Such characteristics may be detectable spectroscopically as an indicator of local morphology.

Projections onto atomic orbitals confirm that rippling mixes in-plane p_x and p_y character into the p_z states. This weakens the π bonds and leads to smaller π - π^* splitting, while simultaneously increasing the in-plane σ bond strength (accordingly, the C-C bond length decreases by $\sim 2\%$ for $\lambda = 6.8 \text{ \AA}$). The smaller π - π^* splitting translates to more accessible states at energies near the Fermi level, which is beneficial for capacitance. A similar rationale can be provided for the scaling of C_q^{int} in the strained samples (Fig. 6). In the case of rippling, there is also some mixing of s character for energies above E_F (negative bias). This contributes to the soft shoulder and the π^* peak splitting seen in the inset of Fig. 7. These result from curvature-induced sp^2 -to- sp^3 rehybridization. For the low-curvature (long-wavelength) samples, the onset of s character is buried beneath the π^* peak, which explains why the soft shoulder at negative bias appears only for shorter wavelengths. Higher curvature introduces more rehybridization; accordingly, the higher-curvature regions of the ripple contribute the most to the capacitive enhancement. This is shown explicitly in the inset of Fig. 7. Note that the carbon at the midway point between two ripple peaks still shows an increase in the density of states with respect to the pristine graphene baseline; we believe this is an artifact of our small sample size.

As a final morphological feature, we examined the

effect of introducing a periodic fold into the graphene framework. Unlike the ripple, the folded sample contains both a graphite-like region in the fold center and a rippled region at its edge, and can be thought of as a maximum corrugation limit. Such folds have been observed in real graphene samples, and are thought to be low-energy transformations of the pristine sheet.^{48,49} The capacitance change, as calculated within the fixed-band approximation, is shown in Fig. 8. Here, we show the total capacitance change, along with the equivalent quantity projected onto each carbon atom along the path from highest to lowest curvature within the fold. As with the rippled sample, the results show an enhancement in capacitance, with the regions of highest curvature contributing most. However, the enhancement is not symmetric about zero bias, but is seen preferentially at negative voltages. This agrees with tight-binding calculations on a single graphene fold.⁵⁰ Atomic orbital projection reveals this to be a π^* feature. There is an analogous contribution from the π states; however, it appears deeper in the valence ($E - E_F = -2.2 \text{ eV}$), and contributes less strongly to the capacitance in the $\pm 1.5 \text{ V}$ window shown in Fig. 8. This is the reason for the asymmetric bias response. Note that this is similar to the asymmetry in the π/π^* response in the polarized ESM results of Fig. 3.

The fold also induces metallicity, which leads to additional capacitive increases near zero bias. This effect has been reported previously, both in calculations and experiments.⁴⁸ The large difference between the capacitive behavior of the fold (Fig. 8) and the ripple (Fig. 7) is somewhat surprising, given their structural similarity. The origin is the graphite-like stacking in the folded sample, which introduces hybridization of the π states between successive layers.⁵⁰ This difference highlights the large influence of local morphology on the electronic structure of real electrodes.

IV. CONCLUSIONS

In conclusion, we have introduced and evaluated strategies for improving the capacitance of graphene-derived supercapacitors that are based on modifying the local structure and morphology of the electrode rather than global surface area and pore geometry. To do so, we have calculated the quantum capacitance within the fixed-band approximation of a variety of defective graphene-based surfaces containing point defects, as well as local strain and curvature. Our calculations confirm that the interfacial capacitance of graphene-derived electrodes is generally limited by the quantum capacitance, which is a consequence of the low density of states near the Fermi level. However, the addition of defects into the graphene structure can significantly improve the calculated capacitance if introduced in sufficient concentrations. For instance, the presence of hydrogen at vacancy-derived nanopores can increase the capacitance near zero bias significantly, whereas Stone-Wales

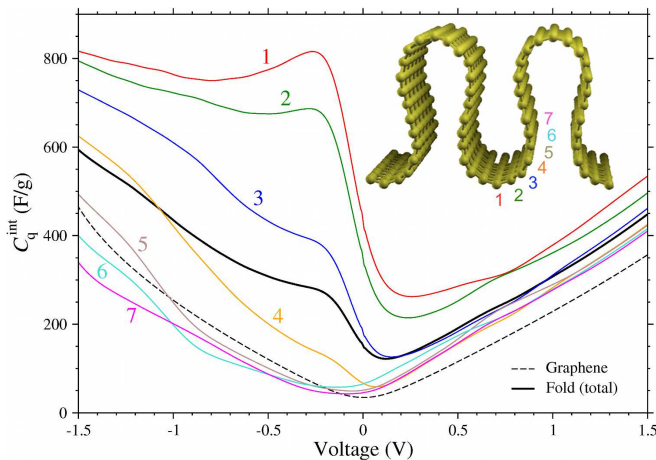


FIG. 8: Theoretical area-specific integrated quantum capacitance C_q^{int} of graphene upon folding the surface as shown in the inset. The total difference is shown alongside spatial projections onto carbon atoms along the edge of the fold. The corresponding carbon atom locations are also shown in the inset.

defects have a much larger effect at higher voltage magnitudes. These could prove an important tool for increasing graphene-based supercapacitor performance. Similarly, tensile strain and rippling upon compression tend to increase capacitance at higher voltage magnitudes. Folding the graphene sheet also increases capacitance, but only at positive potentials. Heavily curved local morphologies, which introduce rippling, folding, and regions of local tensile strain, should therefore be desirable over planar geometries. An in-depth analysis of the electrode screening properties reveals that multilayer regions are far more effective at screening the double-layer potential than are single-layer regions, which leads to higher area-specific capacitance. In this regard, four graphene layers ought to be sufficient to expect nearly full screening. However, the thickness consideration should be weighed against the importance of gravimetric capacitance, which decreases with thickness. Our analysis shows that the fixed-band approximation, in which the density of states is assumed to be rigidly shifted with changes in electronic occupation, remains reliable for single-layer samples but breaks down for multilayer samples due to level splitting and rehybridization of the π^* states. It should be noted that our calculations do not account for the interdependence of the electrode and electrolyte contributions to the capacitance, or for the electrode stability; a more detailed study to this effect is currently underway.

V. ACKNOWLEDGMENTS

Funding was provided by Lawrence Livermore National Laboratory Directed Research and Development (LDRD) Grant 12-ERD-035 and the Japan-U.S. Cooper-

ation Project for Research and Standardization of Clean Energy Technologies. Computing support came from the LLNL Institutional Computing Grand Challenge program. This work was performed under the auspices of the U.S. Department of Energy by LLNL under Contract DE-AC52-07NA27344.

- ¹D. A. C. Brownson, D. K. Kampouris, and C. E. Banks, *Chem. Soc. Rev.* **41**, 6944 (2012).
- ²S. L. Candelaria, Y. Shao, W. Zhou, X. Li, J. Xiao, J.-G. Zhang, Y. Wang, J. Liu, J. Li, and G. Cao, *Nano Energy* **1**, 195 (2012).
- ³D. Chen, L. Tang, and J. Li, *Chem. Soc. Rev.* **39**, 3157 (2010).
- ⁴E. Frackowiak, *Phys. Chem. Chem. Phys.* **9**, 1774 (2007).
- ⁵J. Biener, M. Stadermann, M. Suss, M. A. Worsley, M. M. Biener, K. A. Rose, and T. F. Baumann, *Energy Environ. Sci.* **4**, 656 (2011).
- ⁶A. Pandolfo and A. Hollenkamp, *J. Power Sources* **157**, 11 (2006).
- ⁷J. Chmiola, G. Yushin, Y. Gogotsi, C. Portet, P. Simon, and P. L. Taberna, *Science* **313**, 1760 (2006).
- ⁸R. K. Kalluri, M. M. Biener, M. E. Suss, M. D. Merrill, M. Stadermann, J. G. Santiago, T. F. Baumann, J. Biener, and A. Striolo, *Phys. Chem. Chem. Phys.* **15**, 2309 (2013).
- ⁹H. Gerischer, *J. Phys. Chem.* **89**, 4249 (1985).
- ¹⁰H. Gerischer, R. McIntyre, D. Scherson, and W. Storck, *J. Phys. Chem.* **91**, 1930 (1987).
- ¹¹F. Chen, Q. Qing, J. Xia, J. Li, and N. Tao, *J. Am. Chem. Soc.* **131**, 9908 (2009).
- ¹²H. Shi, *Electrochim. Acta* **41**, 1633 (1996).
- ¹³O. Barbieri, M. Hahn, A. Herzog, and R. Kötz, *Carbon* **43**, 1303 (2005).
- ¹⁴C. Liu, Z. Yu, D. Neff, A. Zhamu, and B. Z. Jang, *Nano Lett.* **10**, 4863 (2010).
- ¹⁵M. Hahn, M. Baertschi, O. Barbieri, J.-C. Sauter, R. Kötz, and R. Gallay, *Electrochim. Sol. State Lett.* **7**, A33 (2004).
- ¹⁶J. Biener, S. Dasgupta, L.-H. Shao, D. Wang, M. A. Worsley, A. Wittstock, J. R. Lee, M. M. Biener, C. Orme, S. O. Kucheyev, B. C. Wood, T. M. Willey, A. V. Hamza, J. Weissmüller, H. Hahn, and T. F. Baumann, *Adv. Mater.* **24**, 5083 (2012).
- ¹⁷P. Giannozzi *et al.*, *J. Phys. Condens. Mat.* **21**, 395502 (2009).
- ¹⁸D. Vanderbilt, *Phys. Rev. B* **41**, 7892 (1990).
- ¹⁹J. P. Perdew, K. Burke, and M. Ernzerhof, *Phys. Rev. Lett.* **77**, 3865 (1996).
- ²⁰M. Otani and O. Sugino, *Phys. Rev. B* **73**, 115407 (2006).
- ²¹J. O. Bockris, A. K. N. Reddy, and M. E. Gamboa-Aldeco, *Modern Electrochemistry 2A: Fundamentals of Electrodeics (Second Edition)* (Springer, 2001).
- ²²B. Roling and M. Drüschler, *Electrochim. Acta* **76**, 526 (2012).
- ²³H. Wang and L. Pilon, *Electrochim. Acta* **76**, 529 (2012).
- ²⁴H. Wang and L. Pilon, *Electrochim. Acta* **64**, 130 (2012).
- ²⁵M. D. Stoller, C. W. Magnuson, Y. Zhu, S. Murali, J. W. Suk, R. Piner, and R. S. Ruoff, *Energy Environ. Sci.* **4**, 4685 (2011).
- ²⁶J. Xia, F. Chen, J. Li, and N. Tao, *Nature Nanotech.* **4**, 505 (2009).
- ²⁷T. Fang, A. Konar, H. Xing, and D. Jena, *Appl. Phys. Lett.* **91**, 092109 (2007).
- ²⁸R. Gillen and J. Robertson, *Phys. Rev. B* **82**, 125406 (2010).
- ²⁹H. Xu, Z. Zhang, and L.-M. Peng, *Appl. Phys. Lett.* **98**, 133122 (2011).
- ³⁰L. A. Ponomarenko, R. Yang, R. V. Gorbachev, P. Blake, A. S. Mayorov, K. S. Novoselov, M. I. Katsnelson, and A. K. Geim, *Phys. Rev. Lett.* **105**, 136801 (2010).
- ³¹M. Sprinkle, D. Siegel, Y. Hu, J. Hicks, A. Tejeda, A. Taleb-Ibrahimi, P. Le Fèvre, F. Bertran, S. Vizzini, H. Enriquez, S. Chi-ang, P. Soukiasian, C. Berger, W. A. de Heer, A. Lanzara, and E. H. Conrad, *Phys. Rev. Lett.* **103**, 226803 (2009).
- ³²R. S. Deacon, K.-C. Chuang, R. J. Nicholas, K. S. Novoselov, and A. K. Geim, *Phys. Rev. B* **76**, 081406 (2007).

- ³³Y. Zhang, Y.-W. Tan, H. L. Stormer, and P. Kim, *Nature* **438**, 201 (2005).
- ³⁴M. Orlita, C. Faugeras, P. Plochocka, P. Neugebauer, G. Martinez, D. K. Maude, A.-L. Barra, M. Sprinkle, C. Berger, W. A. de Heer, and M. Potemski, *Phys. Rev. Lett.* **101**, 267601 (2008).
- ³⁵P. E. Trevisanutto, C. Giorgetti, L. Reining, M. Ladisa, and V. Olevano, *Phys. Rev. Lett.* **101**, 226405 (2008).
- ³⁶A. H. Castro Neto, F. Guinea, N. M. R. Peres, K. S. Novoselov, and A. K. Geim, *Rev. Mod. Phys.* **81**, 109 (2009).
- ³⁷E. A. Henriksen and J. P. Eisenstein, *Phys. Rev. B* **82**, 041412 (2010).
- ³⁸A. F. Young, C. R. Dean, I. Meric, S. Sorgenfrei, H. Ren, K. Watanabe, T. Taniguchi, J. Hone, K. L. Shepard, and P. Kim, *Phys. Rev. B* **85**, 235458 (2012).
- ³⁹F. Giannazzo, S. Sonde, V. Raineri, and E. Rimini, *Nano Lett.* **9**, 23 (2009).
- ⁴⁰S. Dröscher, P. Roulleau, F. Molitor, P. Studerus, C. Stampfer, K. Ensslin, and T. Ihn, *Appl. Phys. Lett.* **96**, 152104 (2010).
- ⁴¹S. Dröscher, P. Roulleau, F. Molitor, P. Studerus, C. Stampfer, K. Ensslin, and T. Ihn, *Phys. Scr.* **2012**, 014009 (2012).
- ⁴²J. C. Meyer, C. Kisielowski, R. Erni, M. D. Rossell, M. F. Crommie, and A. Zettl, *Nano Lett.* **8**, 3582 (2008).
- ⁴³P. A. Denis and F. Iribarne, *J. Mol. Struct.: THEOCHEM* **907**, 93 (2009).
- ⁴⁴E. J. Duplock, M. Scheffler, and P. J. D. Lindan, *Phys. Rev. Lett.* **92**, 225502 (2004).
- ⁴⁵J. M. Carlsson and M. Scheffler, *Phys. Rev. Lett.* **96**, 046806 (2006).
- ⁴⁶S.-M. Choi, S.-H. Jhi, and Y.-W. Son, *Phys. Rev. B* **81**, 081407 (2010).
- ⁴⁷G. Tsoukleri, J. Parthenios, K. Papagelis, R. Jalil, A. C. Ferrari, A. K. Geim, K. S. Novoselov, and C. Galiotis, *Small* **5**, 2397 (2009).
- ⁴⁸K. Kim, Z. Lee, B. D. Malone, K. T. Chan, B. Alemán, W. Regan, W. Gannett, M. F. Crommie, M. L. Cohen, and A. Zettl, *Phys. Rev. B* **83**, 245433 (2011).
- ⁴⁹Z. Liu, K. Suenaga, P. J. F. Harris, and S. Iijima, *Phys. Rev. Lett.* **102**, 015501 (2009).
- ⁵⁰Y. Takagi and S. Okada, *J. Phys. Soc. Jpn.* **79**, 033702 (2010).